JCTC Journal of Chemical Theory and Computation

pubs.acs.org/JCTC Article

Defect Tolerance Mechanism Revealed! Influence of Polaron Occupied Surface Trap States on $CsPbBr_3$ Nanocrystal Photoluminescence: *Ab Initio* Excited-State Dynamics

Aaron Forde and Dmitri Kilin*

Cite This: *J. Chem. Theory Comput.* 2021, 17, 7224–7236 Read Online

ACCESS | Metrics & More | Article Recommendations | Supporting Information

ABSTRACT: Lead halide perovskite (LHP) nanocrystals (NCs) show exceptional defect tolerance which has been attributed to their unique electronic structure, where defect energy levels are not introduced inside the fundamental bandgap, and the role of polarons in screening charge carriers from defects. Here, we use *ab initio* atomistic simulations to explore the interplay between various surface chemistries (A = Cs^+, $R'NH_3^+$; X = Br^-, $RCOO^-$) used to passivate a $CsPbBr_3$ NC surface and their impact on the ground-state (GS) and excited-state (ES) photophysical properties. We investigate pristine fully passivated surfaces and A–X vacancy defects that reflect chemical reactions $A^+ + X^- \rightarrow AX$ on the surface, which result in ligand desorption. For each surface configuration, calculations are performed in the GS and lowest ES (L-ES) electronic configurations, approximating polaron formation after photoexcitation. For models with A–X surface vacancies, we find that localized electron surface trap (ST) states emerge ∼100–400 meV below the pristine S_e band in the L-ES configuration due to polaronic nuclear reorganization. Surprisingly, these trap states contribute relatively bright $S_h \rightarrow$ ST spectral features. To test if these surface trap states remain bright in a dynamic (thermal) situation we implement excited-state molecular dynamics simulations. It is found that the surface defected model shows an enhanced nonradiative recombination rate which reduces the photoluminescence quantum yield (PLQY) from 95% for the pristine surface to 75%. This is accompanied by an order of magnitude reduction in PL intensity and a red shift of the transition energy. This study provides more evidence of the defect tolerance of LHP NCs along with evidence of surface trap states contributing to efficient photoluminescence. The observation of relatively bright surface trap states could provide insight into photophysical phenomena, such as size-dependent stretched-exponential photoluminescence decay and Stokes shifts.

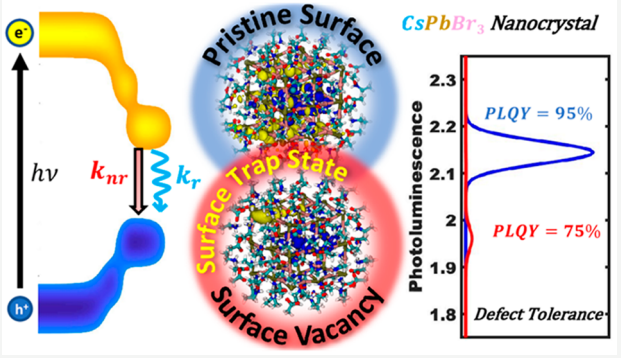

INTRODUCTION

$APbX_3$ (A = Cs, CH_3NH_3; X = I, Br, Cl) lead halide perovskites (LHPs) have become popular materials for a variety of optoelectronic technology applications due to their facile wet-chemical synthesis, tunable chemical composition, and size-dependent photophysical properties. Their versatile and unique electronic properties are largely attributable to their tolerance to crystallographic and surface defects.[1] Traditional semiconductors, such as silicon, show dramatic drops in quantum yields with the introduction of defects due to the formation of deep trap states where the energy of charge carriers is transferred to lattice phonons through nonradiative recombination. LHPs show high efficiencies despite considerable defect densities. Initially, this trend was rationalized in terms of the unique chemical bonding of the Pb–X inorganic network, which shows resistance toward deep-trap-state formation.[2,3] Polarons, quasi-particles that form due to static electron–phonon interactions,[4−6] have also been used to explain the unusually long nonradiative lifetime of charge carriers in bulk films[7,8] and their photoluminescence characteristics.[9,10] Associated with polarons are low-frequency phonon modes that have also been used to rationalize the defect tolerance of LHPs.[11]

LHP nanocrystals[12] (NCs) also show remarkable defect tolerance for both lattice defects and surface point (vacancy) defects. From *ab initio* atomistic simulations, this has been attributed to point defects having fairly large defect formation energies and the energies of electronic states associated with the defects having energies aligning within the conduction/valence band or forming shallow defect states inside the bandgap.[13] TD-DFT has been used to investigate the role of vacancy defects on the optical absorption properties of a $CsPbBr_3$ NC, finding that they are robust to defects, aside from

Received: July 9, 2021
Published: October 19, 2021

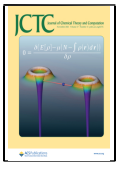

https://doi.org/10.1021/acs.jctc.1c00691
J. Chem. Theory Comput. 2021, 17, 7224–7236

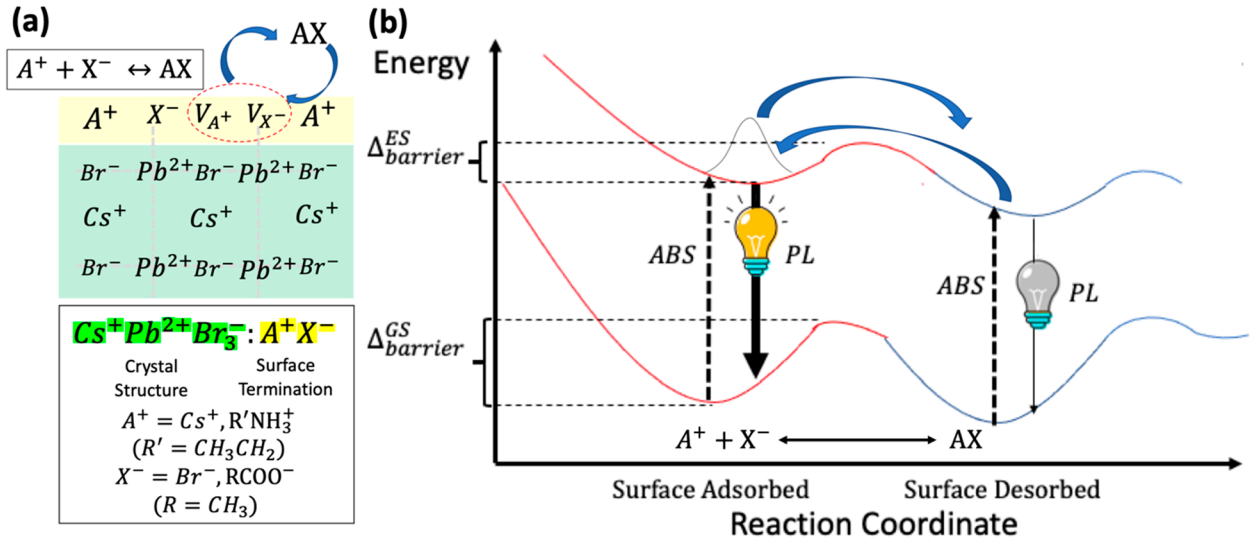

Figure 1. Description of the surface chemistry for $CsPbBr_3$ and the equilibrium that exists between atomic/molecular species that are adsorbed/desorbed from the surface. (a) Diagram illustrating the (100) surface termination of $CsPbBr_3$ resulting in cation A^+ and anion X^- surface ligands adsorbed to surfaces Pb^{2+} and Br^-. For each pair of $A^+$and X^-, there exists an equilibrium between their surface adsorbed state and surface desorbed state: $A^+Br^- + Pb^{2+}X^- \leftrightarrow V_{A^+}\ Br^- + Pb^{2+}\ V_{X^-}$ + AX. For optoelectronic applications, it is preferable to bias the equilibrium toward the surface adsorbed configuration to prevent surface-trap-state formation. (b) For optoelectronic applications, $CsPbBr_3$ nanocrystals are photoexcited and explore the excited-state potential energy surface (PES). A diagram of the PESs is shown in (b). In the adsorbed configuration, it is expected that the nanocrystal will have bright photoluminescence, while in the desorbed configuration, the photoluminescence will become dark.

Br vacancies that introduce trap states that reduce the oscillator strengths and provider lower transition energies compared to pristine NC.[14] These defect tolerances make LHP NCs attractive for commercial luminescence applications, such as LEDs.[15,16]

Atomistic *ab initio* simulations have been shown to be useful in describing the ground-state electronic structure,[17,18] polaronic characteristics,[19,20] and nonradiative dynamics of charge carriers[21] without[22−24] and in the presence of defects[25] in LHPs. Less attention has been paid to vacancy defects under photoexcited and thermal (dynamic) conditions. Under practical operating conditions for optoelectronic applications, LHP NCs will spend a considerable amount of time in the photoexcited state and explore the excited-state potential energy surface (ES-PES). When vacancy defects are present, their energy levels, which remain "hidden" in the conduction/valence band in the ground state, may become stabilized and lower their energy due to polaron occupations (i.e., reorganization energy). Photoexcitation can also potentially catalyze the formation of surface vacancies (i.e., photothermal degradation). This is particularly relevant for LHP NCs, where the surfaces are primarily terminated by cation−anion pairs, some of which are conjugate acid−base pairs,[26] and photoexcitation can act as a catalyst for surface reactions that result in ligand desorption. These considerations will have a direct impact on the description of the photophysical properties of LHP NCs, such as photoluminescence quantum yields (PLQYs), as illustrated in Figure 1. In summary, the role of polaronic occupations in the presence of surface defect sites and the subsequent impact on excited-state dynamics are relatively unexplored. It would be predicted that if polaronic reorganization of energy band alignments resulted in midgap trap states, they would be detrimental to photoluminescence efficiencies.

In this work, we use *ab initio* methodology to study the interplay between electronic configuration (GS and L-ES), surface chemistries, and thermal motion of nuclei in the description of LHP NC optoelectronic properties. The model consists of a Pb−Br-rich $APbX_3$:AX NC surface where we explore three possible A−X surface terminations: alkylammonium alkylcarboxylate ($R'NH_3^+$−$RCOO^-$), alkylammonium bromide ($R'NH_3^+$−Br^-), and cesium alkylcarboxylate (Cs^+−$RCOO^-$). We examine various surface chemistries to see which combinations are likely to form surface vacancies due to chemically induced ligand desorption from the surface. For each passivation scheme, we compute the electronic structure in the GS and L-ES for fully passivated (pristine) and surface vacancy defects that reflect desorption of surface ligands $A^+ + X^- \rightarrow AX$. We find that in the L-ES electronic configuration, regardless of the surface passivation scheme, electron surface trap states emerge inside the pristine bandgap where electron density is localized around surface Pb while the hole remains unaffected by the surface vacancy. To characterize the impact of surface trap states on the photoluminescence properties, we implement nonadiabatic excited-state dynamics, where nonradiative relaxation rates are computed for nonadiabatic couplings and radiative rates are computed from Einstein coefficients. From the excited-state dynamics, we find that the surface defect model shows a high PLQY of 75%, with the pristine surface model having a 95% PLQY.

METHODS

I. Ground-State Electronic Structure Calculations. Noncollinear spin DFT[27,28] is used as the electronic basis, and we include the spin−orbit coupling (SOC) interaction due to the large angular momentum of conduction band Pb^{2+} 6p orbitals. A self-consistent noncollinear spin DFT uses four densities $\rho_{\sigma\sigma'}(\vec{r})$ and rests on the KS equation

$$\sum_{i,\sigma'=\alpha,\beta} (-\delta_{\sigma\sigma'}\nabla^2 + v^{\mathrm{eff}}_{\sigma\sigma'}[\rho_{\sigma\sigma'}(\vec{r})])\varphi_{i\sigma}(\vec{r}) = \varepsilon_i\varphi_{i\sigma'}(\vec{r}) \quad (1)$$

https://doi.org/10.1021/acs.jctc.1c00691
J. Chem. Theory Comput. 2021, 17, 7224−7236

In eq 1, α and β are orthogonal spin indices, and $v^{eff}_{\sigma\sigma'}[\rho_{\sigma\sigma'}(\vec{r})]$ is the 2 × 2 matrix operator of effective potential. In accordance with the self-consistent Kohn−Sham theorem, the 2 × 2 effective potential is a functional of the electronic density for a N_{GS} electron system $v^{eff}_{\sigma\sigma'} = \frac{\delta E^{TOT}[\rho^{N_{GS}}_{\sigma\sigma'}]}{\delta\rho^{N}_{\sigma\sigma'}}$.

Solutions of eq 1 produce spinor Kohn−Sham orbitals (SKSOs), which are two component wave functions composed of a superposition of $|\alpha\rangle$ and $|\beta\rangle$ spin components.

$$\varphi_i^{SKSO}(\vec{r}) = \begin{Bmatrix} \varphi_{i\alpha}(\vec{r}) \\ \varphi_{i\beta}(\vec{r}) \end{Bmatrix} = \varphi_{i\alpha}(\vec{r})|\alpha\rangle + \varphi_{i\beta}(\vec{r})|\beta\rangle \tag{2}$$

As a starting point, we determine the optimized ground-state geometry, in the absence of defects, within the self-consistent DFT with N_{GS} electrons. This corresponds to the following mixed quantum-classical expression:

$$H_e^{N_{GS}}(r) + H_{ph}(R) + H_{e-ph}^{static}(r, R) = H_{SKSO}^{N_{GS}}(r; R) \tag{3}$$

where $H_{SKSO}^{N_{GS}}(r;R)$ describes the electronic and nuclear degrees of freedom where the total energy depends parametrically on the nuclear coordinates R. This defines finding the minima of the potential energy surface (PES) with nuclear coordinates $R_{equilib}^{N_{GS}}$ for the N_{GS} electron system.

To approximate the lowest excited state (L-ES), simulating the lowest energy photoexcitation, we fix electronic occupations so that what would normally be the highest occupied SKSO has a lack of electron density (i.e., a hole) and the lowest unoccupied SKSO contains electron density. This redistribution of charge density will provide new forces acting on the nuclei, which will reorganize around the charge density $\rho^{N_{L\text{-}ES}}_{\sigma\sigma'}$ with a change in nuclear coordinates δR

$$H_e^{N_{L\text{-}ES}}(r) + H_{ph}(R) + H_{e-ph}^{static}(r, R) = H_{SKSO}^{N_{L\text{-}ES}}(r; R + \delta R) \tag{4}$$

This term describes finding the minima of the L-ES PES with nuclear coordinates $R_{equilib}^{N_{GS}} + \delta R = R_{equilib}^{N_{L\text{-}ES}}$.

II. Theory: Ground-State Observables. For each model, we computed the electronic density of states DOS as

$$DOS_{SKSO} = \sum_i \delta(\varepsilon - \varepsilon_i^{SKSO} - \epsilon_{Fermi}) \tag{5}$$

where ε_i^{SKSO} is the band eigenenergy and ϵ_{Fermi} is the Fermi level $\epsilon_{Fermi} = \frac{\varepsilon_i^{SKSO,HOMO} + \varepsilon_i^{SKSO,LUMO}}{2}$.

To quantify the changes in bond distances between ions of the geometry optimized structures, we compute partial radial distribution functions (pRDFs) as

$$g(r) = \frac{1}{4\pi r^2} \sum_{IJ} \delta(r - |\vec{R}_I - \vec{R}_J|) \tag{6}$$

where $|\vec{R}_I - \vec{R}_J|$ represents the pairwise distance between specific ion species I and J. For instance, to find contributions of only Pb and Br coordination, this would mean in the summation I = Pb and J = Br. We also quantify changes in nearest neighbor bond angles.

$$g(\theta) = \sum_{IJ} \delta\left(\theta - \cos^{-1}\left(\frac{\vec{R}_I\vec{R}_J}{|\vec{R}_I||\vec{R}_J|}\right)\right) \tag{7}$$

where the angle is determined by the inverse cosine of the dot product between ions $\vec{R}_I$ and $\vec{R}_J$ normalized by the magnitude of the bond lengths $\vec{R}_I$ and $\vec{R}_J$. The cutoff distance is determined from the distance of the first coordination peak of the pRDF.

To dynamically couple electronic and nuclear degrees of freedom, we used adiabatic molecular dynamics (MD). This provides kinetic energy of nuclei to break orthogonality of electronic states. The nuclear degrees of freedom are treated in the CPA approximation with the nuclei following the classical path trajectories. Nuclear contributions H_{ph} are described within the classical path approximation (CPA) where nuclear wave functions are approximated as delta functions $\phi_v(R_I) = \delta(R_I - \langle R_I\rangle)$ with $\langle R_I\rangle = \langle\phi_v|R_I|\phi_v\rangle$ being the expectation value of nuclear position where $|\phi_v\rangle$ are nuclear wave functions. Thus, the phonon part of the Hamiltonian is represented in terms of positions and momenta of nuclei for potential and kinetic energies. The initial velocities of nuclei are scaled to keep a constant temperature, eq 8, with forces acting on the nuclei depending on the

$$\sum_{I=1}^{N^{ion}} \frac{M_I}{2}\left(\frac{d\vec{R}_I}{dt}\bigg|_{t=0}\right)^2 = \frac{3}{2}N^{ion}k_B T \tag{8}$$

$$\frac{d^2}{dt^2}\vec{R}_I = \vec{F}_I(\hat{\rho}^N_{\sigma\sigma'})/M_I \tag{9}$$

$\vec{R}_I$ represents ionic coordinates, M_I mass of the I^{th} nuclei, k_B is the Boltzmann constant, T is temperature, and $\vec{F}_I([\hat{\rho}])$ is the force acting on the ions. Along molecular dynamics trajectories, we track coordination numbers through time-resolved pRDFs

$$g(r, t) = \frac{1}{4\pi r^2} \sum_{IJ} \delta(r - |\vec{R}_I(t) - \vec{R}_J(t)|) \tag{10}$$

and at each time step integrate up to the first coordination peak r_{bond} to give the average time-dependent coordination number $n_{bond}(t)$

$$n_{bonds}(t) = 4\pi \int_0^{r_{bond}} dr\, r^2 g(r) = \frac{1}{N_I N_J} \sum_{IJ} \int_0^{r_{bond}} dr\, \delta(r - |\vec{R}_I(t) - \vec{R}_J(t)|) \tag{11}$$

Surface defect formation energies are computed as

$$E_{DFE} = E_{NC} - (E_{NC+defect} + E_{reaction}) \tag{12}$$

where $E_{DFE} > 0$ indicates that forming surface defects is thermodynamically favorable and $E_{DFE} < 0$ indicates that forming surface defects is thermodynamically unfavorable. $E_{reaction}$ takes into account the chemical potential of the surface desorbed species.

III. Theory: Reduced Density Matrix Equation of Motion for Electronic Degrees of Freedom. The time evolution of electronic degrees of freedom that are weakly coupled to a thermal bath can be described using the Redfield quantum master equation[29,30] in the density matrix formalism. Typical implementation of Redfield approach assumes the Markov approximation, where the model is immersed into a heat bath so that the bath temperature is constant as the bath is infinitely larger than the model of explicit interest.

https://doi.org/10.1021/acs.jctc.1c00691
J. Chem. Theory Comput. 2021, 17, 7224−7236

$$\frac{\mathrm{d}}{\mathrm{d}t}\hat{\rho} = -\frac{\mathrm{i}}{\hbar}\sum_{k}(F_{ik}\rho_{kj} - \rho_{ik}F_{kj}) + \left(\frac{\mathrm{d}\rho_{ij}}{\mathrm{d}t}\right)_{diss} \tag{13}$$

where F is the many-electron Fock matrix, which includes exchange and correlation, and ρ is the density matrix. The first term is the Liouville−von Neumann equation describing the unitary time evolution of a closed system, while the second term describes electronic energy dissipation due to weak coupling to a thermal bath. For the current model, we are practicing the Redfield equation of motion with a correction to account for the difference of PES on the ground and first excited state. This approach is slightly different from the surface hopping algorithm, which would require the explicit propagation of dynamics along each of the involved excited-state PES. The dissipative transitions result from the quantum part of nuclear kinetic energy. The dissipative transitions are parametrized from NACs computed "on-the-fly" in the basis of SKSO orbitals

$$\begin{aligned}\hat{V}_{ij}^{\mathrm{NA}}(t) &= -\mathrm{i}\hbar\left\langle \varphi_i^{SKSO}(\vec{r}, \{\vec{R}_I(t)\})\left|\frac{\partial}{\partial t}\right|\varphi_j^{SKSO}(\vec{r}, \{\vec{R}_I(t)\})\right\rangle \\ &= -\frac{\mathrm{i}\hbar}{2\Delta t}\int \mathrm{d}\vec{r}\ \{\varphi_{i\alpha}^{*}(\vec{r}, \{\vec{R}_I(t)\}) \quad \varphi_{i\beta}^{*}(\vec{r}, \{\vec{R}_I(t)\})\} \\ &\quad \cdot\begin{Bmatrix}\varphi_{j\alpha}(\vec{r}, \{\vec{R}_I(t+\Delta t)\})\\ \varphi_{j\beta}(\vec{r}, \{\vec{R}_I(t+\Delta t)\})\end{Bmatrix} + h.\,c\end{aligned} \tag{14}$$

The nonadiabatic couplings are precomputed along equilibrium adiabatic molecular dynamics under constraint of the excited state. We highlight that in the limit of $\Delta t \to 0$, this expression reduces to the orthogonality relation $\delta_{ij} = \begin{cases}1, & i = j\\ 0, & i \neq j\end{cases}$. Due to the nuclear kinetic energy of nuclei, the orthogonality relation is broken and provides a "mixing" of SKSOs. NACs are converted into rates of transitions by taking the Fourier transform of the autocorrelation function, which provides components for the Redfield tensor. The Redfield tensor controls the dissipative dynamics of the density matrix. From the Redfield tensor R_{ijkl}, we can approximate a nonradiative recombination rate k_{nr} from Redfield matrix elements

$$k_{nr} \approx R_{\mathrm{HO-LU}} \tag{15}$$

Note that we employ an independent particle approximation where the full dynamics of the electron occupations ρ_c and hole occupations ρ_v

$$\frac{\partial}{\partial t}\begin{pmatrix}\rho_v\\ \rho_c\end{pmatrix} = \begin{pmatrix}R_{vv} & R_{vc}\\ R_{cv} & R_{cc}\end{pmatrix}\begin{pmatrix}\rho_v\\ \rho_c\end{pmatrix} \tag{16}$$

are decoupled such that intraband valence-to-valence nonradiative transitions R_{vv} and conduction-to-conduction R_{cc} are computed, while interband valence-to-conduction R_{vc} and conduction-to-valence R_{vc} transitions are neglected based on the large time scale differences between carrier cooling (ps) and nonradiative recombination (ns). To introduce the effect of nonradiative recombination, we implement a dampening factor $\tilde{\rho}_v = \rho_v e^{-R_{vc}t}$, $\tilde{\rho}_c = \rho_c e^{-R_{cv}t}$)

$$\frac{\partial}{\partial t}\begin{pmatrix}\tilde{\rho}_v\\ \tilde{\rho}_c\end{pmatrix} = \begin{pmatrix}R_{vv} & 0\\ 0 & R_{cc}\end{pmatrix}\begin{pmatrix}\tilde{\rho}_v\\ \tilde{\rho}_c\end{pmatrix} \tag{17}$$

IV. Theory: Excited-State Observables: Charge Distributions, Rates, Absorption Spectra, Photoluminescent Quantum Yields. We use the independent orbital approximation (IOA) in which excited states are described as a pair of orbitals, as opposed to a superposition of orbitals commonly used in TDDFT or Bethe−Saltpeter approaches. Optical transitions between SKSO i and j can be found through transition dipole matrix elements, eq 18, which can be used to compute oscillator strengths, eq 19.

$$\langle\vec{D}_{ij}\rangle = e\int \mathrm{d}\vec{r}\ \{\varphi_{i\alpha}^{*} \quad \varphi_{i\beta}^{*}\}\vec{r}\begin{Bmatrix}\varphi_{j\alpha}\\ \varphi_{j\beta}\end{Bmatrix} \tag{18}$$

$$f_{ij} = |\vec{D}_{ij}|^2\frac{4\pi m_e \nu_{ij}}{3\hbar e^2} \tag{19}$$

where ν_{ij} represents the transition frequency between SKSO i and j'. The transition frequency ν_{ij} is related to the transition energy ΔE_{ij} by $h\nu_{ij}=\Delta E_{ij}$. With known oscillator strengths, an absorption spectrum can be computed through eq 20

$$\begin{aligned}\alpha^{SKSO}(\varepsilon) &= \sum_{i\le \mathrm{HO}}\sum_{j\ge \mathrm{LU}} f_{ij}\delta(\varepsilon - \Delta\varepsilon_{ij}) \\ &= \sum_{i<j} f_{ij}\delta(\hbar\omega - \hbar\omega_{ij})\{\rho_{ii}^{eq} - \rho_{jj}^{eq}\}\end{aligned} \tag{20}$$

Partial contributions of bright transitions from orbitals occupied at equilibrium $\rho_{ii}^{eq} \approx 1$, $i \le$ HO to orbitals unoccupied at equilibrium $\rho_{jj}^{eq} \approx 0$, $j \ge$ LU.

Time-resolved emission in the excited state can be found based on the presence of inverse occupations along the excited-state trajectory and the intensity of oscillator strength between states i and j.

$$E(\hbar\omega, t) = \sum_{j>i} f_{ij}\delta(\hbar\omega - \hbar\omega_{ij})\{\rho_{jj}(t) - \rho_{ii}(t)\} \tag{21}$$

An emission spectrum can be generated by integrating the time-resolved emission along the trajectory

$$E^{tot}(\hbar\omega) = \frac{1}{T}\int_0^T E(\hbar\omega, t)\,\mathrm{d}t \tag{22}$$

Rates of radiative recombination k_r can be found from Einstein coefficients for spontaneous emission[31]

$$k_r = A_{\mathrm{HO-LU}} = \frac{8\pi^2 \nu_{\mathrm{HO-LU}}{}^2 e^2}{\varepsilon_0 m_e c^3}\frac{g_i}{g_j}f_{\mathrm{HO-LU}} \tag{23}$$

$f_{\mathrm{HO-LU}}$ is the oscillator strength, $\nu_{\mathrm{HO-LU}}{}^2$ represents the transition frequency for the HO−LU transition where i = HO and j = LU, g_I is the degeneracy of the electronic state, and the rest of the variables represent the fundamental constants. From the radiative recombination rate k_r and k_{nr}, we compute a PLQY

$$\mathrm{PLQY} = \frac{k_r}{k_r + k_{nr}} \tag{24}$$

V. Computational and Atomistic Details. From the bulk $CsPbBr_3$ crystal structure, 2 × 2 × 2 unit cells carved out, giving Pb/Br terminated surfaces providing a composition of

https://doi.org/10.1021/acs.jctc.1c00691
J. Chem. Theory Comput. 2021, 17, 7224−7236

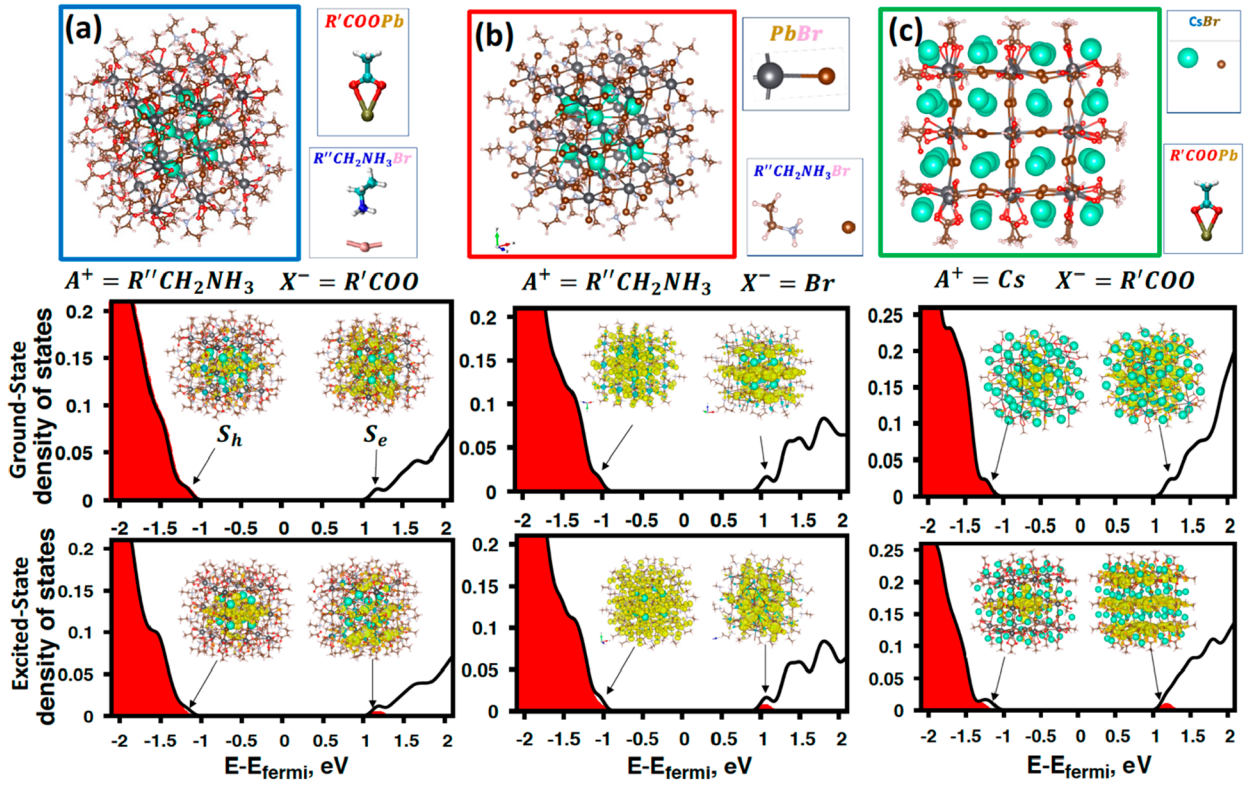

Figure 2. Description of three possible surface chemistries used to passivate the surface of $CsPbBr_3$ nanocrystals and their corresponding electronic density of states in the ground-state (middle row) and lowest-excited-state (bottom row) electronic configurations. (a) Alkylammonium carboxylate, (b) alkylammonium bromide, and (c) cesium carboxylate surface passivation schemes. Insets for the density of states figures are the corresponding spinor Kohn−Sham orbitals (SKSOs) for the S_h and S_e bands. S_h and S_e refer to the spherical symmetry of the envelope function for SKSO, where the charge density is delocalized throughout the interior of the nanocrystal and decays at the boundary. Each surface passivation scheme results in an open bandgap with no shallow or midgap trap states for the ground-state and excited-state electronic configurations.

$Cs_8Pb_{27}Br_{54}$. The surface is composed of the Pb−Br terminated surface. To passivate terminal Pb^{2+} atoms, we use either methylcarboxylate or bromide to occupy the surface X^- lattice sites, and either ethylammonium cations or cesium atoms are used to coordinate to surface Br in the cation A^+ lattice sites. Overall, this gives a structure of $Cs_8Pb_{27}Br_{54}$ passivated with 54 (48) carboxylate/bromide anions (ethylammonium/cesium cations). The original structure deviates from ideal stoichiometry $A_x^+B_x^{2+}C_{3x}^-$, which was fixed by charge balance to open the bandgap with all models having a 2+ charge.[32] This composition gives an NC that has an edge length of ∼2 nm.

The ground-state electronic structure of our atomistic model was found using DFT with the generalized gradient approximation (GGA) Perdew−Burke−Ernzerhof (PBE) functional[33] in a plane-wave basis set along with projector augmented-wave (PAW) pseudopotentials[34,35] in VASP[36] software.

We perform geometry optimization on the ground-state and lowest-excited-state potential energy surfaces, where the lowest-excited state corresponds to the lowest energy photoexcitation. Both optimizations are computed with the GGA functional with subsequent single point calculations where done using noncollinear spin DFT including the SOC interaction which were used to compute observables of the system. All calculations were performed at the Γ point. A simulation cell size of 31 Å × 31 Å × 31 Å with 7 Å of vacuum in each direction. The model is surrounded by a vacuum.

To initialize MD, the NC model was set to a Nose−Hoover thermostat and heated to 300 K. Once the temperature was reached, the MD trajectory was propagated for 1 ps using Δt = 1 fs timesteps under the *NVT* ensemble.

To compute the average coordination number along the MD trajectory from time-resolved pRDFs, we use the following distance cutoffs for integration: r_{Pb-Br} = 5 nm, r_{N-H} = 1.3 nm, and r_{O-H} = 1. 3 nm. These represent the distances where the first coordination peak is fully integrated over and before having a contribution from the second coordination peak.

For computing defect formation energies the chemical potential is considered in the $E_{reaction}$ term which represents the chemical products of the surface leaving group where the defect is created. For example, when considering a vacancy defect for the $R'NH_3$−Br passivation scheme we use the energy of the products of the leaving group $R'NH_3^+ + Br^-$ as the chemical potential $E_{reaction} = E(HBr) + E(R'NH_2)$ which are computed with the same theory (functional and spin−orbit coupling corrections) as the nanocrystal model.

RESULTS

Electronic Structure. In Figure 2(a)−(c), we investigate the ground-state (GS) and the lowest-excited-state (L-ES) electronic structure for three possible surface chemistries to passivate the nanocrystal surface: (a) alkylammonium alkylcarboxylate ($R'NH_3^+$−$RCOO^-$), (b) alkylammonium bromide ($R''NH_3^+$−Br^-), and (c) cesium alkylcarboxylate (Cs^+−$RCOO^-$). The top row shows the GS optimized models, the middle row shows the GS DOS, and the bottom row shows

https://doi.org/10.1021/acs.jctc.1c00691
J. Chem. Theory Comput. 2021, 17, 7224−7236

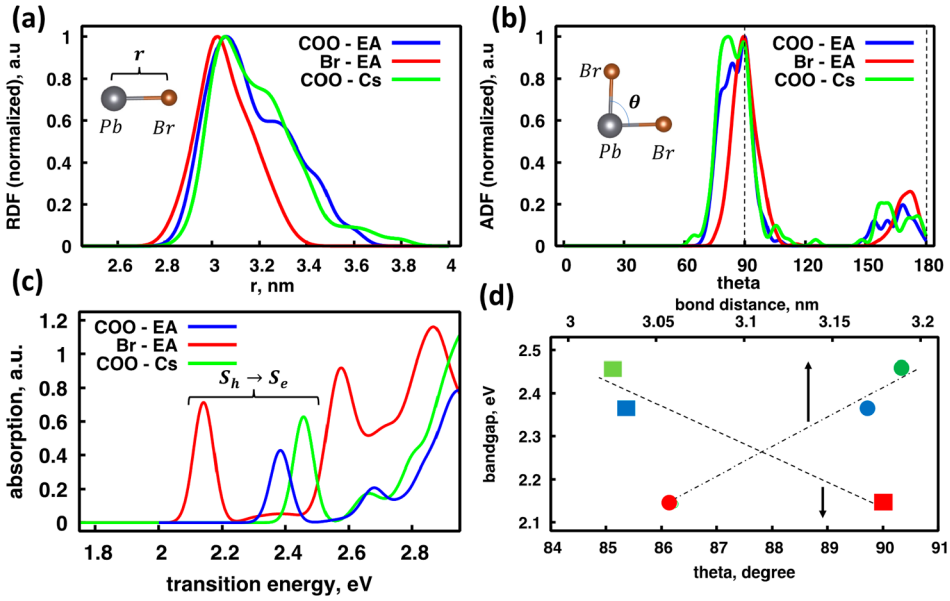

Figure 3. Structure−property relation between the influence of surface chemistry on Pb−Br coordination and the bandgap. (a) Radial distribution of Pb−Br bonds and (b) angular distribution of Pb−Br−Pb coordination for alkylammonium carboxylate (blue), alkylammonium bromide (red), and cesium carboxylate (green) surface passivation. Surfaces containing carboxylates (green, blue) show a broader distribution of radial and angular coordination than those without carboxylates (red). (c) Ground-state absorption spectra for each respective model. Surfaces containing carboxylates also show a larger bandgap, signified by the $S_h \rightarrow S_e$ inset, than those without carboxylates. (d) Expectation value of the Pb−Br−Pb bond angle (bottom, squares, dashed line) and radial bond distance (top, circles, dash-dot line) versus the bandgap for each model. The color scheme is the same as in (a)−(c). The bandgap increases with increasing deviation from ideal octahedral bond angles of 90° and with increasing Pb−Br bond distances. This is attributed to the carboxylates introducing strain on the surface Pb^{2+}, resulting in the breaking of ideal octahedral coordination.

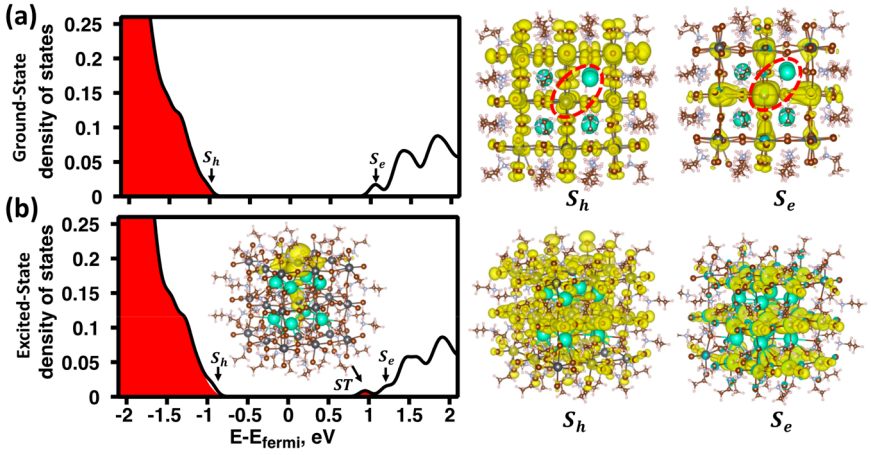

Figure 4. Impact of surface defects on the electronic DOS for the alkylammonium bromide passivated surface. The surface of the $CsPbBr_3$ NC is altered to reflect the following chemical reaction: $R'NH_3^+Br^- + Pb^{2+}Br^- \leftrightarrow V_{A^+}Br^- + Pb^{2+}V_{X^-} + R'NH_2 + HBr$, which results in the surface having an undercoordinated Pb^{2+} and Br^-. This is done by manually removing $R'NH_3^+$ and Br^- from the surface and reoptimizing the geometry in either the ground-state or lowest-excited-state configuration. (a) Density of states for the ground-state and (b) excited-state electronic configurations with specific SKSOs shown. In (a), the locations of surface defects are circled with red dashed lines. The appearance of the shallow trap states on the excited-state PES is a consistent feature that is observed for the alkylammonium carboxylate and cesium carboxylate surface chemistries (see Figures S3−S5).

the L-ES DOS. Insets for the DOS show the corresponding S_h and S_e spinor Kohn−Sham orbitals (SKSOs), where the labels S_x signify that the envelope function of the SKSO is expected to be delocalized within the interior or the NC and decay at the boundary. For each surface passivation scheme, it is observed that the bandgaps are "clean" and free from midgap/shallow trap states where electronic density is localized near the surface. This is confirmed by analysis of the highest occupied and lowest unoccupied SKSOs where their charge density is delocalized throughout the interior of the NC core, as expected for the S_h and S_e electronic states.

Investigating the contribution of surface passivation to the electronic DOS further, we looked at partial DOS (pDOS) for each model (Figure S1). In general, we find that the X^- anions form chemical bonds with surface Pb^{2+}atoms, while the A^+ cations are ionically bound to the surface and do not participate in bond formation. In the valence band, we find that SKSOs are composed of Br−4p and Pb−6s atomic orbitals

https://doi.org/10.1021/acs.jctc.1c00691
J. Chem. Theory Comput. 2021, 17, 7224−7236

for the NC core with contributions from the surface Figure S1(a)(c) O−2p or Figure S1(b) Br−4p orbitals. In the conduction band, the SKSOs are composed primarily of NC core Pb−6p atomic orbitals with contributions from surface O−2p or Br−4p. orbitals.

Surface Chemistry Induced Structure−Property Relationship. In Figure 3(a)−(d), we identify a structure−property relationship between the electronic bandgap of the NC as a function of the surface passivation. Namely, carboxylates binding to surface Pb introduce lattice distortions that result in breaking of ideal Pb−Br bond distances and angles, which increases the bandgap with increasing distortion. Figure 3(a),(b) shows radial distribution functions of Pb−Br bond distances and angular distribution functions for Pb−Br−Pb bond angles for $R''H_3^+$−$RCOO^-$ (blue), $R''NH_3^+$−Br^- (red), and Cs^+−$RCOO^-$(green). In a pristine $CsPbBr_3$ crystal, the Pb atoms form octahedral coordination with Br with expected bond angles of 90° and 180° with a uniform distribution of Pb−Br distances. For the geometry-optimized atomistic models, it is observed that the $R''NH_3^+$−Br^- terminated surface has a near symmetric distribution of Pb−Br bond distances and symmetric Pb−Br−Pb bond angles at 90°, while the $R''NH_3^+$−$RCOO^-$ and Cs^+−$RCOO^-$ surfaces show a skewed distribution of Pb−Br bond distances and Pb−Br−Pb bond angles. Figure 3(c) shows the computed absorption spectrum for each model, which shows that the absorption onset, characterized as a $S_h \rightarrow S_e$ transition, shows a distribution of bandgap values ranging from 2.12 to 2.46 eV. In Figure 3(d), we plot the expectation value of Pb−Br bond distances (top scale, circles) and Pb−Br−Pb bond angles (bottom scale, squares) versus the bandgap. There is a consistent correlation between the deviation from ideal octahedral coordination due to Pb−$RCOO^-$ bonds on the surface and an increased bandgap.

Impact of Surface Vacancy on Electronic Structure and Optical Spectra. In Figure 4(a),(b), we investigate the impact of surface defects on the optoelectronic properties of the NC models. We consider two sites for defect formation: the "face" position on the (100) crystal facet and an "edge" position on the (110) facet. The defects are chosen to reflect the following chemical reactions that are likely to occur on the surface for the (i) $R'NH_3^+$−$RCOO^-$, (ii) $R'NH_3^+$−Br^-, and (iii) Cs^+−$RCOO^-$ terminated surfaces:

$$R'NH_3^+Br^- + Pb^{2+}RCOO^- \leftrightarrow V_{A^+}Br^- + Pb^{2+}V_{X^-} + R'NH_2 + RCOOH \quad (i)$$

$$R'NH_3^+Br^- + Pb^{2+}Br^- \leftrightarrow V_{A^+}Br^- + Pb^{2+}V_{X^-} + R'NH_2 + HBr \quad (ii)$$

$$Cs^+Br^- + Pb^{2+}RCOO^- \leftrightarrow V_{A^+}Br^- + Pb^{2+}V_{X^-} + Cs(RCOO) \quad (iii)$$

where V_A^+ and V_X^- represent vacancy defects at the A^+ and X^- lattice sites. For each surface defect, the geometry is reoptimized in the GS or L-ES configuration. Here, we will focus on defect formation on the face of the $R'NH_3^+$−Br^- terminated surface. In Figure 4(a), we show the GS DOS along with the corresponding S_h and S_e SKSOs. We illustrate where the surface vacancy sites V_A^+ and V_X^- have a red dotted circle where there is an undercoordinated Pb^{2+} surface atom and a vacant A^+ site. We observe that the bandgap remains pristine with no signs of localization of the electronic density near the surface. However, when the geometry is optimized in the L-ES configuration, we observe the appearance of an electronic state within the bandgap, as shown in Figure 4(b). This emergent electronic state is revealed to be a shallow surface defect state where the electronic density of the SKSO is localized on the undercoordinated surface Pb^{2+}, shown as an inset. The formation surface defect states inside the bandgap in the L-ES configuration is a general trend that is observed for the $R''NH_3^+$−$RCOO^-$ and Cs^+−$RCOO^-$ terminated surfaces, as observed in Figures S3 and S4.

To investigate the impact of shallow-trap-state formation on the optical absorption spectra, we compute transition dipoles, using the independent orbital approximation, for models optimized with the GS and L-ES configurations. In Figure 5(a)−(c), we plot the absorption spectra for pristine (red), GS with a face defect (green), GS with an edge defect (blue), ES with a face defect (magenta), and ES with an edge defect (teal) for (a) $R'NH_3^+$−$RCOO^-$, (b) $R'NH_3^+$−Br^-, and (c) Cs^+−$RCOO^-$ terminated surfaces. The main observation is that for all the models and defects considered, the $S_h \rightarrow S_e$ transition remains relatively bright, but when considering the surface defect models optimized in the L-ES configuration, new optical features emerge lower in energy than the $S_h \rightarrow S_e$ transitions. These emergent low-energy transitions are characterized as $S_h \rightarrow$ ST. Interestingly, it is observed that these trap-state facilitated absorption features are relatively bright, where it is generally assumed that surface states will be optically dark.

To assess the thermodynamic stability of each surface chemistry configuration, we compute defect formation energies (DFEs) for each model in the GS and L-ES configurations, as shown in Table 1. The DFEs are computed with respect to the chemical potential of product formation for the chemical reactions described in (1)−(3). Negative (positive) DFEs correspond to the surface adsorbed (desorbed) configuration being more energetically favorable. In the GS configuration, it is found that the $R''NH_3^+$−Br^- and Cs^+−$RCOO^-$ surfaces prefer the surface adsorbed configuration, while the $R''NH_3^+$−$RCOO^-$ surface prefers the desorbed configuration.

Photothermal Stability. To test the photothermal stability of the LHP NC against surface defect formation, we implemented molecular dynamics on pristine, fully passivated NCs in the GS and L-ES electronic configuration at cryogenic (77 K) and room (300 K) temperatures for the $R''NH_3^+$−$RCOO^-$ passivated surface. It is expected that the reaction barrier for ligand desorption from the surface should be reduced in the L-ES compared to the GS due to the increased contribution of repulsive antibonding Pb-6p atomic orbitals. To characterize the transition from the surface adsorbed to desorbed configuration, we track Pb−O coordination numbers along the MD trajectories through the use of RDFs. Integrating the RDF up to the first coordination peak gives the expectation value of Pb−O coordination at the surface at each time step. To track changes in surface chemistry, namely, conversion of ammoniums to amines and carboxylates to carboxylic acids, we also compute N−H and O−H coordination numbers along the trajectory. There is an equilibrium between protonated alkylammonium $R''NH_3^+$ and unprotonated alkylamine $R''NH_2$, which is facilitated by interaction with the strong base $RCOO^-$. Increases (decreases) in O−H (N−H) coordination are signatures of proton transfer occurring through reaction (ii). In Figure 6, we show the coordination number of (a) Pb−O bonds, (b) N−H bonds, and (c) O−H

https://doi.org/10.1021/acs.jctc.1c00691
J. Chem. Theory Comput. 2021, 17, 7224−7236

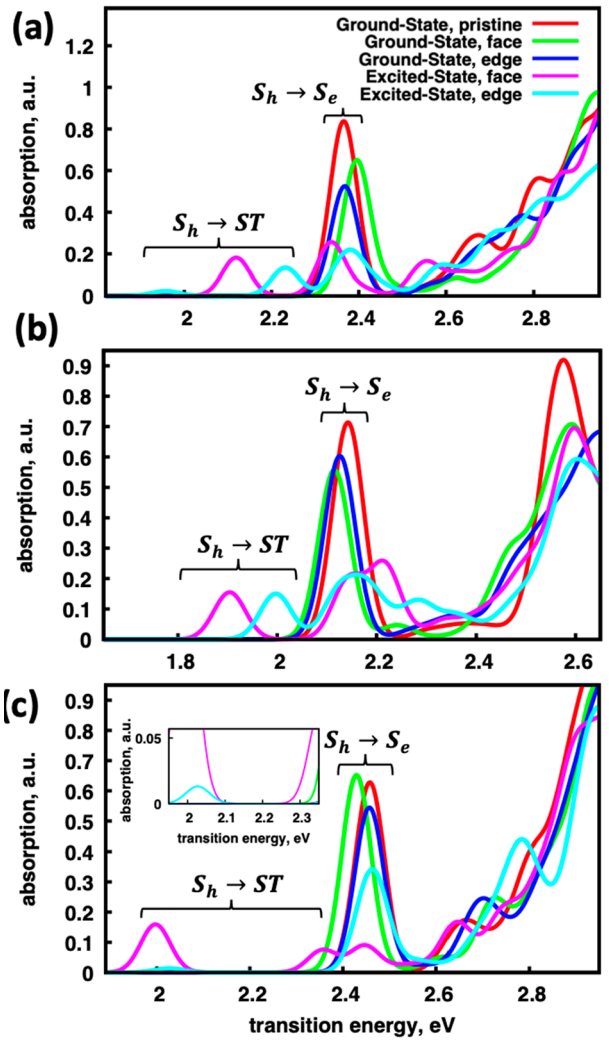

Figure 5. Impact of surface defects on the optical properties. Comparison of the UV−vis absorption spectra for pristine (red), GS with a face defect (green), GS with an edge defect (blue), ES with a face defect (magenta), and ES with an edge defect (teal) for (a) alkylammonium carboxylate, (b) alkylammonium bromide, (c) and cesium carboxylate surface passivation schemes. The main observation is that for the pristine and surface defect models optimized on the GS PES (red, green, blue), the lowest energy transition is $S_h \rightarrow S_e$, while for the surface defect models optimized on the ES PES (magenta, teal), the lowest energy transitions are $S_h \rightarrow$ ST due to the emergence of surface trap states. Interestingly, some of the $S_h \rightarrow$ ST states are relatively bright in absorption.

Table 1. Defect Formation Energies (DFEs, eV) Computed for the Various Surface Chemistries at Various Sites on the NC Surface[a]

defect site	(i) R′NH3−Br	(ii) R′NH3−RCOO	(iii) Cs−RCOO
face	−1.39	1.05	−1.12
edge	−1.39	1.11	−0.75

[a]Positive (negative) binding energies indicate that forming surface defects is thermodynamically favorable (unfavorable).

along a 2 ps trajectory for GS-MD at 300 K (green), ES-MD at 77 K (red), and ES-MD at 300 K (black). The ES-MD(77K) trajectory shows essentially no change in Pb−O coordination and no changes in N−H or O−H coordination. The GS-MD(300K) and ES-MD(300K) trajectories show decreasing Pb−O coordination numbers accompanied by decreasing (increasing) N−H (O−H) coordination. This indicates that proton transfer on the surface helps promote the desorption of carboxylates and ammonium from the surface, consequently leaving surface vacancy sites. This analysis agrees with the computed DFE formation energies from Table 1, where the desorbed configuration is thermodynamically favored.

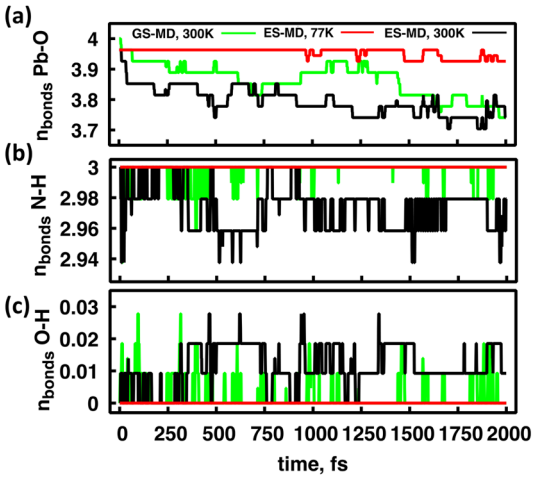

Figure 6. Change in (a) Pb−O, (b) N−H, and (c) O−H coordination numbers along GS-MD at 300 K (green) and ES-MD trajectories at either 77 K (red) or 300 K (black) for the $R'NH_3^+$−$RCOO^-$ passivated NC model. Coordination numbers are computed from the time-resolved radial distribution function $g[r(t)]$ and integrated up to the first coordination peak to give $n_{bonds}(t)$. From (a), it is observed that for the ES-MD(77K) there are small changes in Pb−O coordination while for the GS-MD(300K) and ES-MD(300K) trajectories show a continuous decrease in Pb−O coordination numbers, with small oscillations along the trajectory. For (b) and (c), it is also observed that there are no changes in N−H or O−H coordination numbers for the ES-MD(77K) trajectory, while the GS-MD(300K) and ES-MD(300K) trajectories show changes. A decrease in N−H coordination signifies conversion from ammonium to amine, and an increase in O−H coordination signifies conversion from carboxylate to carboxylic acid. This indicates that chemical reactions facilitated by proton transfer occur on the surface where carboxylates are converted to carboxylic acids, which have much less attraction to surface Pb, resulting in photothermal surface degradation.

Excited-State Dynamics. Last, we implement nonadiabatic excited-state dynamics to examine the influence of surface vacancy defects on the photoluminescent properties of the $R'NH_3^+$−Br^- surface passivated NC models. Specifically, we look to see if the bright-trap-state absorption observed in Figure 5 is robust to thermal fluctuations and shows bright PL. We compute nonadiabatic couplings and transition dipoles along the GS MD trajectory for the pristine NC and along the L-ES MD trajectory for an NC with surface vacancies on the face of the NC at 77 K, with SKSO band fluctuations shown in Figure S5(a),(b).

From the SKSO band fluctuations for the pristine surface model, it is observed that the fluctuations are fairly small and that the S_e and S_h electronic bands show substantial subgaps. For the surface defective model, Figure S5(b), it is observed that initially, there are two trap states below the S_e electronic band. After 75 fs, the trap-state energies either merge into states in the conduction band or become a shallow trap state slightly lower in energy than the S_e electronic band, resembling

https://doi.org/10.1021/acs.jctc.1c00691
J. Chem. Theory Comput. 2021, 17, 7224−7236

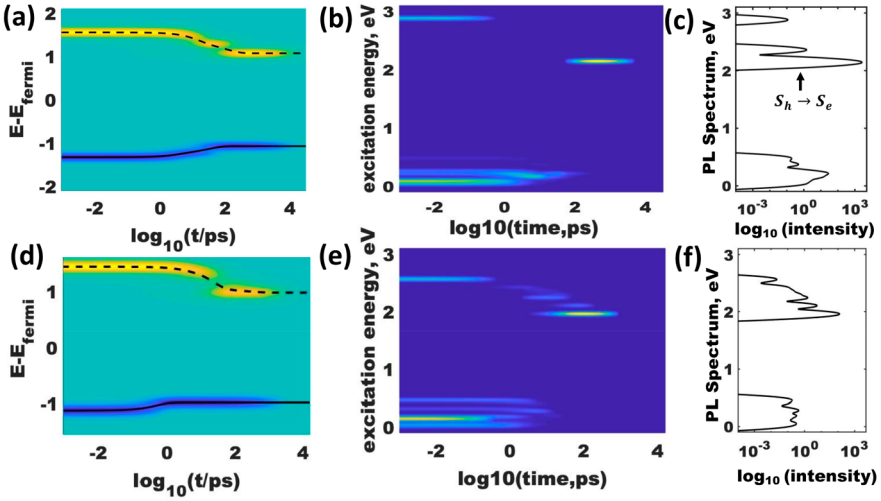

Figure 7. Nonadiabatic excited-state dynamics trajectories for (a)−(c) the pristine and (d)−(f) the face-defect R′NH_3^+−Br^- terminated surfaces. (a) and (d) describe the nonradiative relaxation with initial conditions representing photoexcitation. The yellow (blue) lines represent the nonequilibrium charge density of the photoexcited electron (hole), and the dotted (solid) line represents the average energy of the electron (hole). (b),(c) and (e),(f) describe radiative relaxation along the trajectory with (b),(e) being time-resolved and (c),(f) time-integrated photoluminescence. For the pristine model, once the charge carriers relax to the lowest-excited-state energy, there is bright photoluminescence from $S_h \rightarrow S_e$. For the face-defect model, the charge carriers relax to the lowest-excited-state energy, and as the photoexcited electron passes through the S_e electronic level, there is bright photoluminescence from the $S_h \rightarrow$ ST transition.

the band fluctuations of the pristine surface. At 175 fs shallow trap states start to reemerge.

Nonadiabatic couplings computed along the MD trajectory are processed into time-averaged state-to-state nonradiative transition rates, illustrated in Figure S5(c),(d). Initial conditions for the dynamics being chosen based on the most intense optical excitations. Radiative transitions during the excited-state trajectory are computed from time-average oscillator strengths $1/T\sum_{ij} f_{ij}$, which compete with nonradiative transitions R_{iijj}. Figure 7(a)−(c) shows the (a) nonradiative, Figure 7(b),(c) shows the radiative dynamics for the pristine R′NH_3^+−Br^- surface passivated NC model, and Figure 7(d)−(f) shows the (d) nonradiative and (e) and (f) radiative dynamics for the NC with a face defect. For the nonradiative dynamics, the yellow (blue) lines represent the nonequilibrium charge density of the photoexcited electron (hole), and the dotted (solid) line represents the average energy of the electron. (hole). Changes in population occupations for each band are shown in Figure S6. For the radiative dynamics, Figure 7(b),(e) describes the time-resolved photoluminescence and Figure 7(c),(f) describes the time-integrated photoluminescence.

For Figure 7(a), the nonradiative dynamics for the pristine surface, we see that after photoexcitation, the charge carriers nonradiatively relax to the S_h and S_e energy levels on the time scale of 10^2 ps and nonradiatively decay across the bandgap on the time scale of 10^4 ps. Changes in the SKSO occupations of holes in the valence band and electrons in the conduction band are shown. Along the same trajectory, radiative relaxation events occur, as shown in Figure 7(b),(c), which occur before and after the charge carriers relax to the S_h and S_e energy levels. The early events are hot photoluminescence, and after 10^2 ps, the luminescence is from the $S_h \rightarrow S_e$ transition. From Figure 7(c), we see that the dominant radiative channel is the $S_h \rightarrow S_e$ transition, as it has the longest lifetime.

The nonradiative dynamics for the face-defect model, Figure 7(d), show similarities and differences to the pristine model, Figure 7(a). First, we will remark that the average electronic band energies for the surface defect model are similar to those of the pristine surface model due to the ST states oscillating between being "inside" the bandgap and "hidden" in the conduction bands (see SI Figure 5(a),(b)). With this methodology, we average over the states where the ST state is below and above the S_e band. The similarity between the pristine and surface defect models is that the hot-electron cooling rates k_e are very similar, while the hot-hole cooling rate k_h is 2 orders of magnitude faster for the surface defect model than for the pristine model, as observed in Table 2. The radiative recombination dynamics, shown in Figure 7(e),(f), for the surface defect model are also similar to those of the pristine surface model. The main difference is that the PL transition energy is ≈200 meV below the pristine surface PL and that the PL intensity of the surface defect model is an order of magnitude lower than that of the pristine surface model. This was attributed to the surface defect model having

Table 2. Summary of Radiative and Nonradiative Relaxation Dynamics from the Excited-State Dynamics

HO-x	LU+y	OS	k_r [1/ns]	k_{nr} [1/ns]	PLQY
		Pristine Surface, 77 K			
HO	LU	1.22	3.03	0.13	0.96
HO-1	LU	1.07	2.66	0.13	0.95
HO	LU+1	0.85	2.12	0.15	0.93
HO-1	LU+1	0.73	1.81	0.13	0.93
average	0.97	2.41	0.13	0.95	
		Surface Defect, 77 K			
HO	LU	1.06	2.20	0.75	0.75
HO-x	LU+y	ΔE_{diss}	k_h [1/ps]	k_e [1/ps]	
		Pristine Surface, 77 K			
HO-8	LU+14	0.74	0.04	0.02	
		Surface Defect, 77 K			
HO-4	LU+8	0.62	2.09	0.02	

https://doi.org/10.1021/acs.jctc.1c00691
J. Chem. Theory Comput. 2021, 17, 7224−7236

a seven times faster nonradiative recombination rate k_{nr} (see Table 2).

From the radiative and nonradiative recombination rates, we compute PLQY, as observed in Table 2. For the pristine surface, there is a 2-fold degeneracy for the HOMO and LUMO states, giving four possible radiative recombination channels. We averaged over the recombination channels and found a PLQY = 95%. In the surface defect model, the degeneracy is broken, and there is only one lowest energy recombination channel, which has a PLQY = 75%. The reduction in the PLQY for the surface defect model is due to an enhanced nonradiative recombination rate k_h, which is seven times faster than the rates for the pristine surface model.

DISCUSSION

Impact of Surface Chemistry on the Bandgap. It has been observed that bulk and nanostructured $A^+B^{2+}X_3^-$ metal halide perovskites have a positive deformation potential $\frac{\partial E_{gap}}{\partial \ln(V)} > 0$.[37−39] In previous reports, the focus is on how changes in the chemical composition of the bulk crystal alter the structural distortion due to the Goldschmidt tolerance factor, which is a measure of how efficient the A^+ cations fill the space created by the $B^{2+}-X^-$ bonding network. Here, the interesting observation, as detailed in Figure 3, is that changes in surface composition alter the bandgap through changes in the Pb−Br bonding network. This is likely due to the difference in how Br^- and $RCOO^-$ coordinate to surface Pb^{2+}. Surface Br^- will have the same coordination bonding as bulk crystal Br^- but the $RCOO^-$ molecules have a distribution of binding configurations,[40] such as monodentate and bidentate, which will be different from the bulk crystal Br^-. This mismatch likely creates strain and breaks the ideal octahedral symmetry bonding network of Pb−Br. We keep in mind that these atomistic models, approximately 2 nm in edge length, are smaller in size than what is typically observed in experiments, typically, 3−15 nm. Therefore, it is likely that these effects are accentuated for smaller NCs due to the larger surface area to volume ratio. The main consequence would be that the bandgap would not strictly follow the commonly used effective mass approximation and that the surface chemistry can result in the EMA underestimating the bandgap.

Defect Formation in the Excited State. Tight-binding types of analysis indicate that halide vacancy defects for lead halide perovskites can provide defect levels which remain inside the manifold of conduction band states[41] and has been supported by DFT calculations.[3]

In the presence of a photoexcitation, shifting of nuclear coordinates stabilizes the defect energy level and "pushes" it inside the bandgap. One may interpret it in a similar way as a solvato-chromic effect: the defect state may have a nonzero static dipole. The polarization/nuclear reorganization/polaronic effect reorganize positions of all ions of the nanocrystal, which serve as a surrounding dielectric media for the defect. Then, the stabilization of energy of such state happens due to medium polarization along force lines of the electric field of the defect.

Role of Proton Transfer on Surface Binding Stability. The surface chemistry of lead halide perovskite nanocrystals, using the original synthesis procedure,[12] has been shown to be one of the main hindrances toward their long-term colloidal stability. It was found that there is a dynamic equilibrium between adsorbed and desorbed configurations of ligands on the NC surface,[42] which over time leads to colloidal instability and precipitation of solution due to aggregation formation. From the *ab initio* molecular dynamics trajectories for the $R''NH_3^+-RCOO^-$ passivated surface, Figure 6, we observe that the coordination of $RCOO^-$ to the surface Pb^{2+} is reduced through protonation by an adjacent $R''NH_3^+$. This agrees with reports of how acid−base equilibria have a strong influence on their colloidal stability.[26,43] This motivates the use of surface chemistries that are unaffected by environmental pH, such as zwitterions[44] and aprotic alkylammoniums.[18]

The defect formation energies reported in Table 1 represent the internal energies which physically represent the interaction of the functional groups of the organic molecules to the perovskite surface. In experiment, long chain oleic acid and oleylamine ligands are used. Here we approximate the organic molecules as short alkyl chain acetate and ethylammonium ions which provide minimal steric hindrance. Hence entropic contributions to the binding energy are neglected. Explicit account for alkyl chains would likely decrease the binding energies but would still be dominated by the internal energies due to large interaction energies at the surface.

An explicit account for solvent molecules would increase the computational cost too dramatically to make these calculations feasible. Typically, in experiment, organic solvents, such as toluene and hexane, are used which interact with surface ligand alkyl chains to provide solvation. The organic solvent has minimal impact on optical properties for these materials,[45] which is the main focus of this study. To some extent the shell of the ligands mimics some features of the solvent and NC itself plays the role of electrostatic medium.

Impact of Surface Vacancy Defect on the Photoluminescence Properties. It is a general expectation that any trap enhances nonradiative recombination and greatly suppresses radiative recombination by quenching the oscillator strength. However, in this particular case, the enhancement of nonradiative recombination is dramatically weaker than one could expect along with a fractional decrease in radiative recombination. There are two factors: (i) the defect is shallow, and recombination through the gap is long, according to the gap law; (ii) the defect is much brighter than a typical defect state. A combination of (i) and (ii) is responsible for the noticeable PLQY, which one can interpret as defect tolerance. In summary, polaronic nuclear reorganization creates the shallow surface trap state. The surface trap state happens to be bright. Experimental samples typically appear as ensembles of nanocrystals with different defect densities. An average over defect free and defected nanocrystals is expected to provide experimental PLQY in the range between computed values. This work identifies a range, where experimental PLQY could be found.

In colloidal $CsPbBr_3$ NCs, there have been reports of stretched exponential PL decay with decreased NC size.[46,47] Single exponential PL decay is considered to come from a two-level system, whereas stretched exponential decay is a signature of a distribution of relaxation pathways. These atomistic simulations help provide insight that bright surface trap states can introduce additional radiative pathways that could be the origin of stretched exponential photoluminescence decay.

Another interesting note is that the surface defect model showed a red-shifted PL transition energy compared to the pristine surface. It has been observed that with decreased NC size (increased surface-to-volume ratio), the Stokes shift increases significantly.[45,48] From the electronic structure

https://doi.org/10.1021/acs.jctc.1c00691
J. Chem. Theory Comput. 2021, 17, 7224−7236

calculations described apart from Figure 4, we find that the trap states emerge only after polaronic nuclear reorganization due to charge carriers occupying the trap state (i.e., after photoexcitation) and that the surface defect model can show relatively bright emission (see Figure 7). Thus, absorption could occur via the $S_h \rightarrow S_e$ transition across the pristine bandgap E_{gap} and then photoluminescence via the $S_0 \rightarrow$ ST transition with transition energy $E_{gap} - E(\mathrm{ST})$, where $E(\mathrm{ST})$ is the reorganization energy of the surface trap state.

CONCLUSIONS

Lead halide perovskite nanocrystals are of interest for their optoelectronic properties. In particular, luminescence sources are used for traditional light-emitting devices and next-generation devices, such as quantum information manipulation and processing. One of the beneficial properties of LHP NCs is their defect tolerance. To date, the ground-state energetics of trap-state formation and electronic structure have been well characterized using *ab initio* atomistic methods, where it is found that lattice and surface point defects generally result in the energy bands contributed by defect sites remaining "hidden" in the valence and conduction bands.

However, in realistic situations, these vacancy sites can be occupied by polaronic charge carriers due to photoexcitation, which can rearrange the alignment of these trap states due to significant nuclear reorganization energies. In this work, we investigate the polaronic occupation of model LHP NCs with pristine surface passivation or vacancy defects and the impact of the surface vacancies on the excited-state dynamics, such as PLQY and recombination rates. We consider multiple possible surface chemistries ($A = Cs^+$, $R'NH_3^+$; $X = Br^-$, $RCOO^-$) to passivate the surface of the LHP NC model.

By examining the ground-state electronic structure of LHP NCs with a fixed edge length of 2 nm and various surface chemistries, we find that the bandgap can be tuned over a range of ~300 meV with each passivation scheme having bright $S_h \rightarrow S_e$ optical transitions. The $R'NH_3^+-Br^-$ terminated surface shows the smallest bandgap, and the $R'NH_3^+/Cs^+-RCOO^-$ passivated surfaces show larger bandgaps. This is attributed to the surface binding of $RCOO^-$ to surface Pb^{2+}, providing lattice strain that increases the bandgap due to its positive deformation potential $\frac{\partial E_{gap}}{\partial \ln(V)} > 0$.

When considering the effect of surface vacancies, represented as ion pairs desorbing from the surface through the chemical reaction $A^+ + X^- \rightarrow AX$, on the electronic structure, we find that in the ground-state configuration, the bandgap remains pristine. However, when considering the lowest-excited-state configuration, approximating photoexcitation by placing an electron in the S_e band and having a hole in the S_h band, surface trap states (ST) emerge inside the bandgap ~100−400 meV below the S_e band. This is attributed to polaronic reorganization. Interestingly, the surface trap states contribute relatively bright $S_h \rightarrow$ ST optical absorption signatures where it is generally assumed that these features would be dark.

To investigate the influence of surface defect vacancies on the LHP NC photoluminescence properties, we implement excited-state dynamics simulations in a density-matrix formalism where nonradiative relaxation is treated using Redfield theory and radiative relaxation is treated using Einstein coefficients for spontaneous emission. The surface defect model shows an enhanced nonradiative recombination rate, which reduces the photoluminescence quantum yield (PLQY) from 95% for the pristine surface to 75%. This is accompanied by an order of magnitude reduction in PL intensity and a redshift of the transition energy.

In total, this study provides more support for the defect tolerance of LHP NCs along with evidence of surface trap states contributing to efficient photoluminescence. The observation of relatively bright surface trap states could provide insight into photophysical phenomena, such as size-dependent stretched-exponential photoluminescence decay and Stokes shifts.

ASSOCIATED CONTENT

Supporting Information

The Supporting Information is available free of charge at https://pubs.acs.org/doi/10.1021/acs.jctc.1c00691.

Partial density of states of each model, pRDF and pADF functions of Pb−Br bonds for the GS and L-ES optimized models, DOS and SKSOs for models with surface defects optimized on the GS and L-ES models, SKSO band fluctuations and Redfield tensors for the RNH_3-Br models used for dynamics, occupation dynamics along the excited-state dynamics trajectory, comparison of the computed PL spectra for the pristine and vacancy defect models (PDF)

Representative trajectories of *ab initio* molecular dynamics (ZIP)

AUTHOR INFORMATION

Corresponding Author

Dmitri Kilin − *Department of Chemistry and Biochemistry, North Dakota State University, Fargo, North Dakota 58102, United States;* orcid.org/0000-0001-7847-5549; Email: dmitri.kilin@ndsu.edu

Author

Aaron Forde − *Department of Materials Science and Nanotechnology, North Dakota State University, Fargo, North Dakota 58102, United States*

Complete contact information is available at: https://pubs.acs.org/10.1021/acs.jctc.1c00691

Notes

The authors declare no competing financial interest.

ACKNOWLEDGMENTS

The authors thank the DOE BES NERSC facility for computational resources, allocation award #91202, "*Computational Modeling of Photo-catalysis and Photo-induced Charge Transfer Dynamics on Surfaces*", supported by the Office of Science of the DOE under contract no. DE-AC02-05CH11231. D.K. acknowledges support of this work by the National Science Foundation through Grant No. CHE-1944921, for methods development. A.F. acknowledges support from NSF CHE-2004197, for exploration of organic−inorganic interfaces. D.K. thanks Svetlana Kilina, Talgat Inerbaev, David Micha, Sergei Tretiak, Oleg Prezhdo, and Yuri Dahnovski for inspiring discussions. Authors thank Yulun Han, Meade Erikson, Amirhadi Alesadi, David Graupner for editorial suggestions.

REFERENCES

(1) Yin, W.-J.; Shi, T.; Yan, Y. Unusual defect physics in CH3NH3PbI3 perovskite solar cell absorber. *Appl. Phys. Lett.* **2014**, *104*, 063903.

(2) Buin, A.; Pietsch, P.; Xu, J.; Voznyy, O.; Ip, A. H.; Comin, R.; Sargent, E. H. Materials Processing Routes to Trap-Free Halide Perovskites. *Nano Lett.* **2014**, *14*, 6281−6286.

(3) Kang, J.; Wang, L.-W. High Defect Tolerance in Lead Halide Perovskite CsPbBr3. *J. Phys. Chem. Lett.* **2017**, *8*, 489−493.

(4) Neukirch, A. J.; Nie, W.; Blancon, J.-C.; Appavoo, K.; Tsai, H.; Sfeir, M. Y.; Katan, C.; Pedesseau, L.; Even, J.; Crochet, J. J.; Gupta, G.; Mohite, A. D.; Tretiak, S. Polaron Stabilization by Cooperative Lattice Distortion and Cation Rotations in Hybrid Perovskite Materials. *Nano Lett.* **2016**, *16* (6), 3809−3816.

(5) Meggiolaro, D.; Ambrosio, F.; Mosconi, E.; Mahata, A.; De Angelis, F. Polarons in Metal Halide Perovskites. *Adv. Energy Mater.* **2020**, *10*, 1902748.

(6) Poncé, S.; Schlipf, M.; Giustino, F. Origin of Low Carrier Mobilities in Halide Perovskites. *ACS Energy Lett.* **2019**, *4*, 456−463.

(7) Zhu, X. Y.; Podzorov, V. Charge Carriers in Hybrid Organic−Inorganic Lead Halide Perovskites Might Be Protected as Large Polarons. *J. Phys. Chem. Lett.* **2015**, *6*, 4758−4761.

(8) Miyata, K.; Meggiolaro, D.; Trinh, M. T.; Joshi, P. P.; Mosconi, E.; Jones, S. C.; De Angelis, F.; Zhu, X. Y. Large polarons in lead halide perovskites. *Science Adv.* **2017**, *3*, e1701217.

(9) Munson, K. T.; Kennehan, E. R.; Doucette, G. S.; Asbury, J. B. Dynamic Disorder Dominates Delocalization, Transport, and Recombination in Halide Perovskites. *Chem.* **2018**, *4*, 2826−2843.

(10) Munson, K. T.; Doucette, G. S.; Kennehan, E. R.; Swartzfager, J. R.; Asbury, J. B. Vibrational Probe of the Structural Origins of Slow Recombination in Halide Perovskites. *J. Phys. Chem. C* **2019**, *123*, 7061−7073.

(11) Chu, W.; Zheng, Q.; Prezhdo, O. V.; Zhao, J.; Saidi, W. A. Low-frequency lattice phonons in halide perovskites explain high defect tolerance toward electron-hole recombination. *Science Adv.* **2020**, *6*, eaaw7453.

(12) Protesescu, L.; Yakunin, S.; Bodnarchuk, M. I.; Krieg, F.; Caputo, R.; Hendon, C. H.; Yang, R. X.; Walsh, A.; Kovalenko, M. V. Nanocrystals of Cesium Lead Halide Perovskites (CsPbX(3), X = Cl, Br, and I): Novel Optoelectronic Materials Showing Bright Emission with Wide Color Gamut. *Nano Lett.* **2015**, *15*, 3692−6.

(13) ten Brinck, S.; Zaccaria, F.; Infante, I. Defects in Lead Halide Perovskite Nanocrystals: Analogies and (Many) Differences with the Bulk. *ACS Energy Lett.* **2019**, *4*, 2739−2747.

(14) Perez, C. M.; Ghosh, D.; Prezhdo, O.; Tretiak, S.; Neukirch, A. J. Excited-State Properties of Defected Halide Perovskite Quantum Dots: Insights from Computation. *J. Phys. Chem. Lett.* **2021**, *12*, 1005−1011.

(15) Kim, Y.; Yassitepe, E.; Voznyy, O.; Comin, R.; Walters, G.; Gong, X.; Kanjanaboos, P.; Nogueira, A. F.; Sargent, E. H. Efficient Luminescence from Perovskite Quantum Dot Solids. *ACS Appl. Mater. Interfaces* **2015**, *7*, 25007−25013.

(16) Yan, F.; Xing, J.; Xing, G.; Quan, L.; Tan, S. T.; Zhao, J.; Su, R.; Zhang, L.; Chen, S.; Zhao, Y.; Huan, A.; Sargent, E. H.; Xiong, Q.; Demir, H. V. Highly Efficient Visible Colloidal Lead-Halide Perovskite Nanocrystal Light-Emitting Diodes. *Nano Lett.* **2018**, *18*, 3157−3164.

(17) Forde, A.; Hobbie, E.; Kilin, D. Role of Pb^{2+} Adsorbents on the Opto-Electronic Properties of a CsPbBr3 Nanocrystal: A DFT Study. *MRS Adv.* **2019**, *4*, 1981−1988.

(18) Bodnarchuk, M. I.; Boehme, S. C.; ten Brinck, S.; Bernasconi, C.; Shynkarenko, Y.; Krieg, F.; Widmer, R.; Aeschlimann, B.; Günther, D.; Kovalenko, M. V.; Infante, I. Rationalizing and Controlling the Surface Structure and Electronic Passivation of Cesium Lead Halide Nanocrystals. *ACS Energy Lett.* **2019**, *4*, 63−74.

(19) Neukirch, A. J.; Abate, I. I.; Zhou, L.; Nie, W.; Tsai, H.; Pedesseau, L.; Even, J.; Crochet, J. J.; Mohite, A. D.; Katan, C.; Tretiak, S. Geometry Distortion and Small Polaron Binding Energy Changes with Ionic Substitution in Halide Perovskites. *J. Phys. Chem. Lett.* **2018**, *9*, 7130−7136.

(20) Forde, A.; Inerbaev, T.; Kilin, D. Spectral Signatures of Positive and Negative Polarons in Lead-Halide Perovskite Nanocrystals. *J. Phys. Chem. C* **2020**, *124*, 1027−1041.

(21) Li, W.; She, Y.; Vasenko, A. S.; Prezhdo, O. V. Ab initio nonadiabatic molecular dynamics of charge carriers in metal halide perovskites. *Nanoscale* **2021**, *13*, 10239−10265.

(22) Li, W.; Zhou, L.; Prezhdo, O. V.; Akimov, A. V. Spin−Orbit Interactions Greatly Accelerate Nonradiative Dynamics in Lead Halide Perovskites. *ACS Energy Lett.* **2018**, *3*, 2159−2166.

(23) Forde, A.; Inerbaev, T.; Hobbie, E. K.; Kilin, D. S. Excited-State Dynamics of a $CsPbBr_3$ Nanocrystal Terminated with Binary Ligands: Sparse Density of States with Giant Spin−Orbit Coupling Suppresses Carrier Cooling. *J. Am. Chem. Soc.* **2019**, *141*, 4388−4397.

(24) Boehme, S. C.; Brinck, S. t.; Maes, J.; Yazdani, N.; Zapata, F.; Chen, K.; Wood, V.; Hodgkiss, J. M.; Hens, Z.; Geiregat, P.; Infante, I. Phonon-Mediated and Weakly Size-Dependent Electron and Hole Cooling in $CsPbBr_3$ Nanocrystals Revealed by Atomistic Simulations and Ultrafast Spectroscopy. *Nano Lett.* **2020**, *20*, 1819−1829.

(25) Li, W.; Long, R.; Tang, J.; Prezhdo, O. V. Influence of Defects on Excited-State Dynamics in Lead Halide Perovskites: Time-Domain ab Initio Studies. *J. Phys. Chem. Lett.* **2019**, *10*, 3788−3804.

(26) Almeida, G.; Goldoni, L.; Akkerman, Q.; Dang, Z.; Khan, A. H.; Marras, S.; Moreels, I.; Manna, L. Role of Acid−Base Equilibria in the Size, Shape, and Phase Control of Cesium Lead Bromide Nanocrystals. *ACS Nano* **2018**, *12*, 1704−1711.

(27) Barth, U. v.; Hedin, L. A local exchange-correlation potential for the spin polarized case. i. *J. Phys. C: Solid State Phys.* **1972**, *5*, 1629−1642.

(28) Kubler, J.; Hock, K. H.; Sticht, J.; Williams, A. R. Density Functional Theory Of Non-Collinear Magnetism. *J. Phys. F: Met. Phys.* **1988**, *18*, 469−483.

(29) Redfield, A. G. On the Theory of Relaxation Processes. *IBM J. Res. Dev.* **1957**, *1*, 19−31.

(30) Jean, J. M.; Friesner, R. A.; Fleming, G. R. Application of a Multilevel Redfield Theory to Electron Transfer in Condensed Phases. *J. Chem. Phys.* **1992**, *96*, 5827−5842.

(31) Einstein, A. On the Quantum Theory of Radiation. *Phys. Z.* **1917**, *18*, 121.

(32) Forde, A.; Inerbaev, T.; Kilin, D. Role of Cation-Anion Organic Ligands for Optical Properties of Fully Inorganic Perovskite Quantum Dots. *MRS Adv.* **2018**, *3*, 3255−3261.

(33) Perdew, J. P.; Burke, K.; Ernzerhof, M. Generalized Gradient Approximation Made Simple [Phys. Rev. Lett. 77, 3865 (1996)]. *Phys. Rev. Lett.* **1997**, *78*, 1396−1396.

(34) Blöchl, P. E. Projector augmented-wave method. *Phys. Rev. B: Condens. Matter Mater. Phys.* **1994**, *50*, 17953−17979.

(35) Kresse, G.; Joubert, D. From ultrasoft pseudopotentials to the projector augmented-wave method. *Phys. Rev. B: Condens. Matter Mater. Phys.* **1999**, *59*, 1758−1775.

(36) Kresse, G.; Furthmuller, J. Efficiency of ab-initio total energy calculations for metals and semiconductors using a plane-wave basis set. *Comput. Mater. Sci.* **1996**, *6*, 15−50.

(37) Frost, J. M.; Butler, K. T.; Brivio, F.; Hendon, C. H.; van Schilfgaarde, M.; Walsh, A. Atomistic Origins of High-Performance in Hybrid Halide Perovskite Solar Cells. *Nano Lett.* **2014**, *14* (5), 2584−2590.

(38) Amat, A.; Mosconi, E.; Ronca, E.; Quarti, C.; Umari, P.; Nazeeruddin, M. K.; Grätzel, M.; De Angelis, F. Cation-Induced Band-Gap Tuning in Organohalide Perovskites: Interplay of Spin−Orbit Coupling and Octahedra Tilting. *Nano Lett.* **2014**, *14*, 3608−3616.

(39) Quarti, C.; Mosconi, E.; De Angelis, F. Interplay of Orientational Order and Electronic Structure in Methylammonium Lead Iodide: Implications for Solar Cell Operation. *Chem. Mater.* **2014**, *26*, 6557−6569.

(40) Kennehan, E. R.; Munson, K. T.; Doucette, G. S.; Marshall, A. R.; Beard, M. C.; Asbury, J. B. Dynamic Ligand Surface Chemistry of

https://doi.org/10.1021/acs.jctc.1c00691
J. Chem. Theory Comput. 2021, 17, 7224−7236

Excited PbS Quantum Dots. *J. Phys. Chem. Lett.* **2020**, *11* (6), 2291−2297.
(41) Brandt, R. E.; Poindexter, J. R.; Gorai, P.; Kurchin, R. C.; Hoye, R. L. Z.; Nienhaus, L.; Wilson, M. W. B.; Polizzotti, J. A.; Sereika, R.; Žaltauskas, R.; Lee, L. C.; MacManus-Driscoll, J. L.; Bawendi, M.; Stevanović, V.; Buonassisi, T. Searching for "Defect-Tolerant" Photovoltaic Materials: Combined Theoretical and Experimental Screening. *Chem. Mater.* **2017**, *29* (11), 4667−4674.
(42) De Roo, J.; Ibanez, M.; Geiregat, P.; Nedelcu, G.; Walravens, W.; Maes, J.; Martins, J. C.; Van Driessche, I.; Kovalenko, M. V.; Hens, Z. Highly Dynamic Ligand Binding and Light Absorption Coefficient of Cesium Lead Bromide Perovskite Nanocrystals. *ACS Nano* **2016**, *10*, 2071−81.
(43) Quarta, D.; Imran, M.; Capodilupo, A.-L.; Petralanda, U.; van Beek, B.; De Angelis, F.; Manna, L.; Infante, I.; De Trizio, L.; Giansante, C. Stable Ligand Coordination at the Surface of Colloidal CsPbBr3 Nanocrystals. *J. Phys. Chem. Lett.* **2019**, *10*, 3715−3726.
(44) Krieg, F.; Ochsenbein, S. T.; Yakunin, S.; ten Brinck, S.; Aellen, P.; Süess, A.; Clerc, B.; Guggisberg, D.; Nazarenko, O.; Shynkarenko, Y.; Kumar, S.; Shih, C.-J.; Infante, I.; Kovalenko, M. V. Colloidal CsPbX3 (X = Cl, Br, I) Nanocrystals 2.0: Zwitterionic Capping Ligands for Improved Durability and Stability. *ACS Energy Lett.* **2018**, *3*, 641−646.
(45) Brennan, M. C.; Herr, J. E.; Nguyen-Beck, T. S.; Zinna, J.; Draguta, S.; Rouvimov, S.; Parkhill, J.; Kuno, M. Origin of the Size-Dependent Stokes Shift in CsPbBr3 Perovskite Nanocrystals. *J. Am. Chem. Soc.* **2017**, *139*, 12201−12208.
(46) Forde, A.; Fagan, J. A.; Schaller, R. D.; Thomas, S. A.; Brown, S. L.; Kurtti, M. B.; Petersen, R. J.; Kilin, D. S.; Hobbie, E. K. Brightly Luminescent $CsPbBr_3$ Nanocrystals through Ultracentrifugation. *J. Phys. Chem. Lett.* **2020**, *11*, 7133−7140.
(47) Li, J.; Gan, L.; Fang, Z.; He, H.; Ye, Z. Bright Tail States in Blue-Emitting Ultrasmall Perovskite Quantum Dots. *J. Phys. Chem. Lett.* **2017**, *8*, 6002−6008.
(48) Brennan, M. C.; Forde, A.; Zhukovskyi, M.; Baublis, A. J.; Morozov, Y. V.; Zhang, S.; Zhang, Z.; Kilin, D. S.; Kuno, M. Universal Size-Dependent Stokes Shifts in Lead Halide Perovskite Nanocrystals. *J. Phys. Chem. Lett.* **2020**, *11*, 4937−4944.

https://doi.org/10.1021/acs.jctc.1c00691
J. Chem. Theory Comput. 2021, 17, 7224−7236